ADVANCED MATERIALS TECHNOLOGIES
www.advmattechnol.de

High Performance Rotary-Structured Triboelectric-Electromagnetic Hybrid Nanogenerator for Ocean Wind Energy Harvesting

Xiaole Cao, Hanlin Zhou, Yuxuan Zhou, Yiran Hu, Yuanyu Wang, Zhong Lin Wang,* and Qijun Sun**

Modern ship is an important transportation and even military equipment on the ocean, which has ubiquitous ocean wind energy with high-speed and stable wind direction. However, much higher-speed wind energy during the movement of the ship is often abandoned. Triboelectric nanogenerator (TENG) that can generate electrical energy by scavenging ambient mechanical energy is one of the emerging energy harvesting technologies. By coupling the TENG and electromagnetic generators (EMG), a high-performance rotary-structured triboelectric-electromagnetic hybrid nanogenerator (RS-HG) is designed in this study. By introducing a matched inductor in the paired energy management circuit (EMC), the charging efficiency of RS-TENG can be effectively enhanced by 15 times compared to that without EMC. At a simulated wind speed of 15 m s^{-1}, the peak power of lateral TENG (L-TENG), top TENG (T-TENG) and EMG are 7.54, 7.85, and 22.5 mW, respectively. The demonstrated RS-HG comprising two RS-TENGs and one EMG can readily charge a 1 mF capacitor to 8 V within 15 s under the wind speed of 15 m s^{-1} and continuously power the electronic devices. Moreover, the RS-HG can also successfully charge a smartphone through the step-down and voltage stabilization module to further expand its application scenarios. The applications of powering portable electronics reveal the huge prospects of hybrid nanogenerators in energy harvesting and self-powered environmental monitoring during navigation.

1. Introduction

Ship is a common way to travel and transport goods in modern society. In recent years, with the increasing level of ship automation, all kinds of new sensors are widely used in the cabin; with the increasing complexity of the shipboard control system, a larger number and more sophisticated sensors are required to be introduced into the whole ship.[1,2] Currently, the power supply to various sensors in the shipboard control systems mainly relies on batteries or electricity generated from fossil fuel energy, which needs to be replaced periodically and may cause environmental pollution issues.[3,4] Therefore, the required numerous sensors on ship call for a type of novel power source that can operate distributedly and continuously in a self-powered fashion to alleviate the above issues. Emerging energy harvesting techniques offer effective strategies to scavenge energy from the ambient environment (e.g., wind, solar, mechanical vibration, and water flow energy).[5–7] As is known, wind energy is a clean, renewable, and widespread natural resource in the environment. The ubiquitous high-speed ocean wind energy during sailing is more favorable to be utilized for the distributed power supply.[8,9] Based on the coupling effect of triboelectricity and electrostatic induction, triboelectric nanogenerator (TENG) can efficiently convert ambient mechanical energy into electrical energy, especially for low-frequency, irregular, and widely

X. Cao, H. Zhou, Y. Zhou, Y. Hu, Z. L. Wang, Q. Sun
Beijing Institute of Nanoenergy and Nanosystems
Chinese Academy of Sciences
Beijing 101400, P. R. China
E-mail: zhong.wang@mse.gatech.edu; sunqijun@binn.cas.cn

X. Cao, Y. Hu, Q. Sun
School of Nanoscience and Technology
University of Chinese Academy of Sciences
Beijing 100049, P. R. China

Y. Wang
College of Materials and Metallurgy
Guizhou University
Guizhou 550025, P. R. China
E-mail: yywang1@gzu.edu.cn

Z. L. Wang
Georgia Institute of Technology
Atlanta, GA 30332, USA

Q. Sun
Shandong Zhongke Naneng Energy Technology Co., Ltd.
Dongying 257061, P. R. China

The ORCID identification number(s) for the author(s) of this article can be found under https://doi.org/10.1002/admt.202300327

DOI: 10.1002/admt.202300327

distributed vibrational energy.[10–12] Thanks to the merits of low cost, lightweight, and high conversion efficiency, the TENG has been intensively demonstrated as a sustainable energy-harvesting technology for capturing the surrounding mechanical energy, especially the low-frequency energy.[13–16]

In this context, geometry design, structures/materials optimization, and energy coupling strategies have been exploited for TENG devices to effectively harvest wind energy.[17,18] As is known, under the same mechanical input, the TENG and conventional electromagnetic generator (EMG) have different output characteristics: the TENG shows a higher voltage, while the EMG shows a higher current.[18,19] Therefore, the hybridization of TENG and EMG can take advantage of their complementary strengths and significantly improve their output performance. Zhu et al. designed a swing-structured hybrid nanogenerator with improved performance and durability, which can be hung on tree branches and exhibit effective energy harvesting on the breeze wind for environmental monitoring.[20] Wu et al. proposed an electrostatic-electromagnetic hybrid generator with greatly enhanced energy conversion efficiency, in which a synchronously controlled voltage multiplier (SCVM) was designed to efficiently store the energy from EMG.[21] Although these demonstrations offer certain advantages for wind energy harvesting, the output performance of TENG component at high-frequency conditions is still low among the reported hybrid nanogenerators. It is mainly because its charging efficiency as well as energy conversion efficiency tend to be poorer than EMG at high-frequency conditions. And its contribution in hybrid nanogenerators is often small despite the high-voltage output characteristics of TENG. Therefore, how to improve the charging efficiency of TENG in hybrid nanogenerators is a key problem.

In this study, a high-performance rotary-structured triboelectric-electromagnetic hybrid nanogenerator (RS-HG) is proposed for ocean wind energy harvesting. By introducing a matched inductor in the paired EMC, the charging efficiency of the TENG component is effectively enhanced, which is significantly increased by 15 times compared to that without EMC. The whole RS-HG consists of two TENGs (top-TENG and lateral TENG) and a bottom EMG. The TENG component is optimized by utilizing polycarbonate (PC) fiber as the triboelectric layer to improve the wear resistance, based on which the output performance can remain stable even after 45 000 cycles. At a simulated wind speed of 15 m s^{-1}, the peak power of L-TENG, T-TENG, and EMG is 7.54, 7.85, and 22.5 mW, respectively. By combining the two TENGs and one EMG, the RS-HG can easily charge a 1 mF capacitor to 8 V within 15 s and continuously power the electronic equipment, exhibiting potential applications in self-powered environmental monitoring during ocean cruises. Moreover, through the step-down and voltage stabilization module, the RS-HG can even successfully charge a smartphone to further expand its application prospect. This study renders an effective approach to harness the enormous energy generated by the high-speed ocean wind energy, enhancing the wind harvesting ability of the RS-HG toward practical application of environmental monitoring and self-power supply during navigation.

2. Results and Discussion

Modern ships are important transportation and military equipment, including cruise ships, cargo ships, destroyers, etc. When they gallop on the ocean where there is ubiquitous ocean wind with higher speed and more stable wind direction compared to land wind, the high-speed wind energy generated during the movement of the ship is often abandoned. The navigation of modern ships relies on a large amount of sensory networks and energy-consuming electronics. Therefore, a cost-effective supplement to the electric power by harvesting the surrounding ocean wind energy during the movement of the ship is urgently needed to meet the power demands of distributed sensory networks and low-power operation of the onboard electronics. Combining the advantages of TENG at low frequency and EMG at high frequency, the hybrid triboelectric-electromagnetic nanogenerator has been demonstrated as an effective power source to drive various electronic devices. Regarding the wide range of wind speed during deep-sea navigation and a long period of high wind speed, the RS-HG for harvesting ocean wind energy is elaborately designed as a power source with high efficiency and sustainability. Schematic illustration of the typical onboard application scenarios of RS-HG as the power source is shown in **Figure 1**a. The all-in-one structured RS-HGs can be installed on the lighthouse or the deck of a cruise ship for readily harvesting the oncoming ocean wind energy. Figure 1b presents the enlarged structure of the RS-HG, which is constituted of two freestanding mode TENGs (T-TENG and L-TENG) and a rotary-structured bottom EMG to fully utilize and harvest the ocean wind energy. As the rotary mode is widely used in the electromagnetic wind turbine for wind energy harvesting with excellent structural stability, high frequency, and high efficiency, the typical rotary structure (including a rotator and a stator) is also adopted to design the TENG and EMG components in the HG. For the T-TENG, the rotor is acrylic with scalloped polycarbonate (PC) fluff, and the stator is fabricated by a commercialized printed circuit board (PCB) with three pairs of crossed-scalloped copper electrodes and a 50 μm thick FEP dielectric layer. For the L-TENG, the stator consists of three pairs of parallel electrodes as the induction electrodes and FEP film as the triboelectric layer, and the rotator is a 3D-printed hub structure with attached PC fluff. For the EMG, the stator is composed of three 5 × 10 rectangular coils (arranged with the angle between two arbitrarily adjacent coils at 120°) fixed in an acrylic plate with grooves, and the rotor is composed of an acrylic plate with six magnets in the same polarity. The three NGs are assembled into the RS-HG with an overall cylindrical exterior and an internal rotor extension shaft that can be connected to various wind cup structures for energy harvesting. The rotator extension shaft is fixedly connected to the rotors of two TENGs and EMG so that they can rotate together following the rotation of the wind cups. The synergistic combination of three generators in the unified structure promises the most effective utilization of external wind energy.

Generally, rotary-structured TENG has a relatively large frictional resistance during its operation and may cause material wear. Introducing a soft-contact dielectric layer between the stator and rotor can effectively reduce the frictional resistance, protect the surface of the charged dielectric layer, and prolong the device

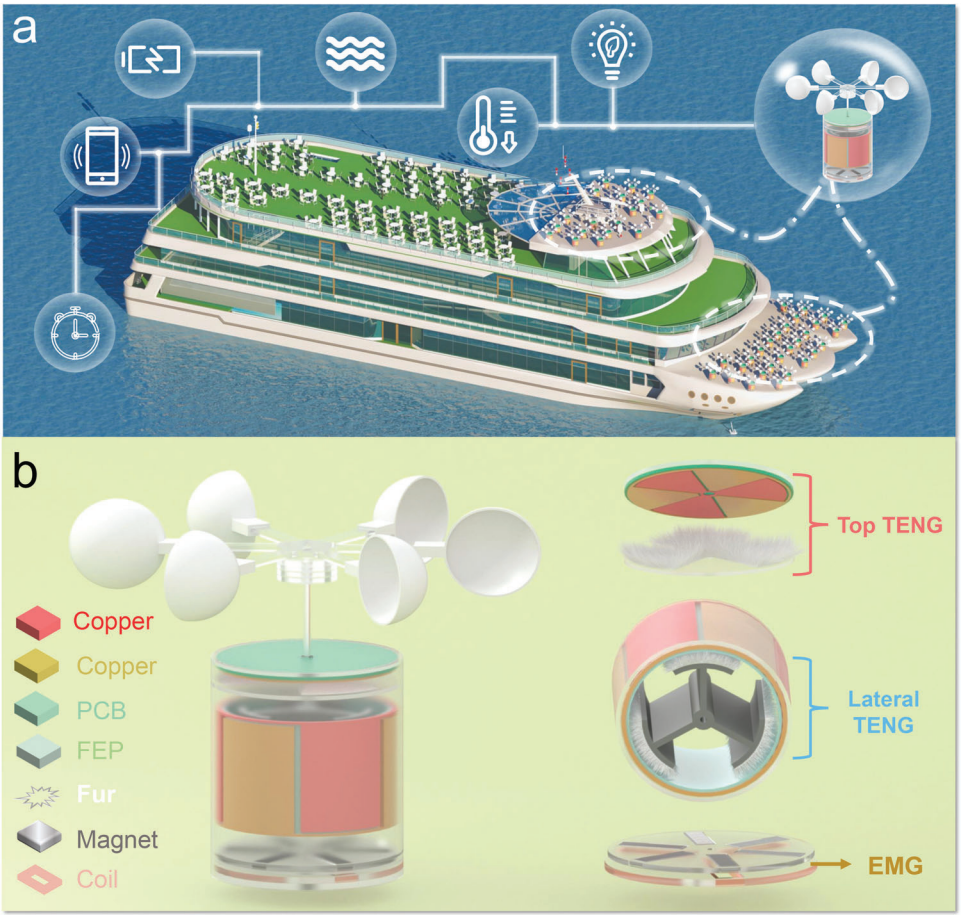

Figure 1. a) Schematic diagram of rotary-structured hybrid nanogenerator (RS-HG) ocean wind energy harvesting. b) Schematic configuration of RS-HG consists of top TENG, lateral TENG, and EMG.

life, which is also capable to improve the output power density of TENG.[6,22,23] To select proper materials for the RS-HG, Figure S1 (Supporting Information) shows the comparison of TENG outputs based on different soft-contact triboelectric layers. Under the same test condition, PC fluff and FEP show the best output performance, demonstrating a high output performance of 1.7 kV, 3.2 μA, and 0.35 μC. Although it is previously reported that rabbit fur has the best output performance,[24] the achieved high output performance from PC fluff in this work is mainly attributed to that PC pluff has a denser and higher number of fibers compared to rabbit fur and results in superior contact. Accordingly, PC fluff is chosen as the dielectric layer for soft contact in our RS-HG.

The working process and operation mechanism of each component in the RS-HG is first explained in **Figure 2**. For the rotary structure TENG, the FEP films and the fan-shaped PC fluff membrane are in good contact and electron transfer occurs on the surface due to electrostatic induction, resulting in positive charge on the PC fluff surface and negative charge on the FEP surface. Owing to the charge conservation, the amount of the induced electrostatic charges on the PC fluff sectors and FEP films are equivalent. Figure 2a shows the typical working cycle of the freestanding TENG, one basic unit is selected to clarify the working mechanism and signal generation.[25] In the initial state (i), the PC fluff brush is placed precisely above the left electrode. Due to the electrostatic induction, appropriate negative free charges are induced on FEP locally above the left electrode to balance the opposite positive polarization on the PC fluff. When the PC fluff sector is rotated anti-clockwise relative to the bottom electrode (states ii), the negative polarization intensity on the left side gradually decreases, while the negative polarization intensity on the right side gradually increases. The free electrons are redistributed from the left electrode to the right electrode through the external circuit until the charges on the left electrode and the FEP film reach the balance again (state iii). When the fan-shaped PC fluff further rotates anti-clockwise and completely passes through the right electrode (iv), the electrons will flow back to the right electrode, generating a current pulse in reversed direction. In the following rotation process, the next fan-shaped PC fluff will cross the two electrodes and continue the above cycles, resulting in the continuous alternating current (AC) output of the rotary structure TENG. Figure 2b shows the COMSOL simulations of the potential distribution under the entire rotation process to assist the understanding of the power generation process.

The EMG component relies on the principle of electromagnetic induction, which can generate periodic AC based on the periodic variation of magnetic flux.[26] As shown in Figure 2c, in the first state (i), the coil is located between the two magnets

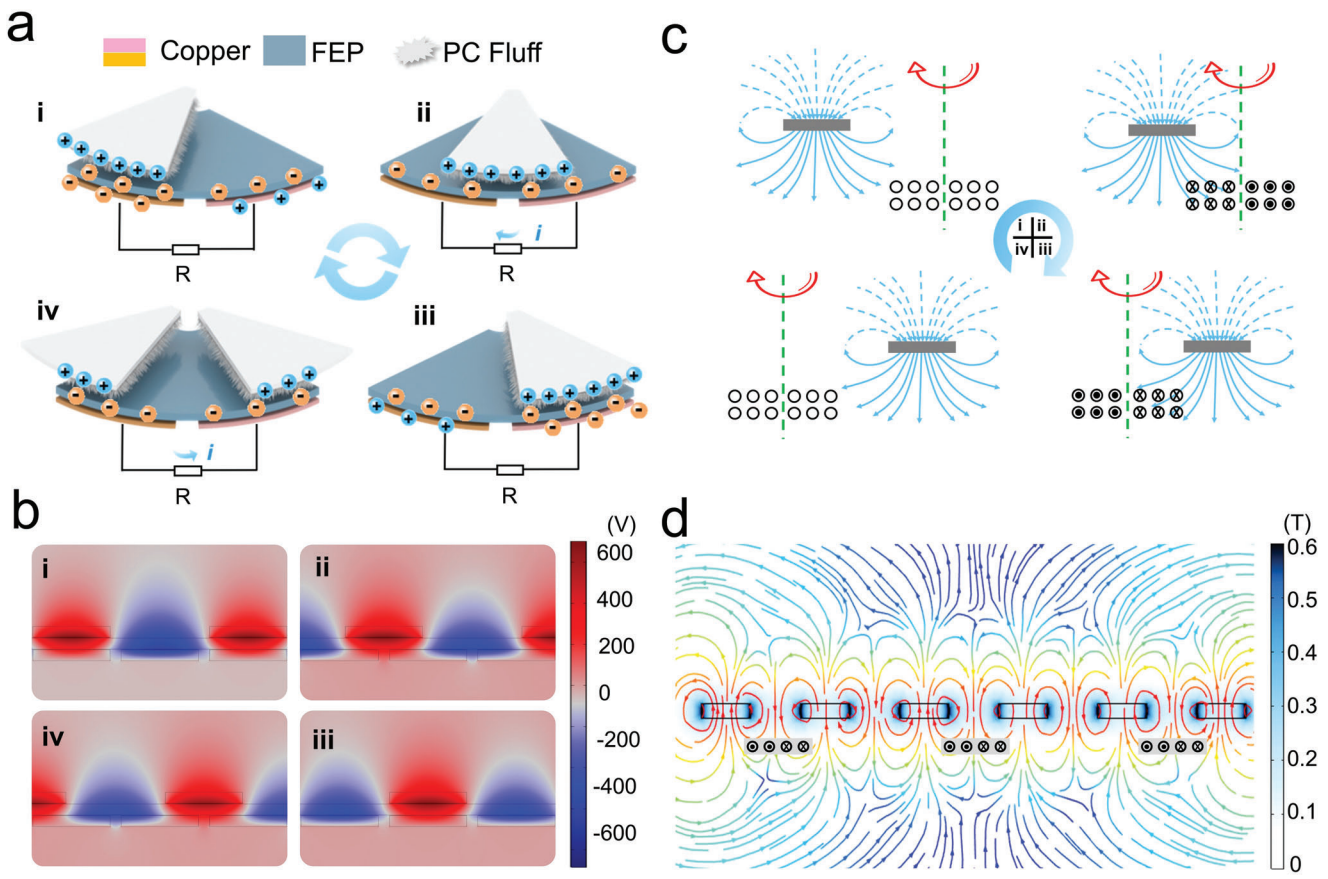

Figure 2. Working mechanism and potential distribution simulation of RS-HG a) schematic diagram of the working principle of the rotary TENG for electrostatic induction in the charge-saturated stage. b) COMSOL simulation results of rotary TENG corresponding to the rotating state c) Simulated distribution of magnetic induction lines of EMG and the direction of coil-induced current at four typical situations. d) The magnetic flux distribution of the magnet in the EMG is simulated by COMSOL.

and the magnetic flux does not change, so the induced current is zero. When the magnet rotates around the axis, the separation distance between the coil and the magnet decreases and the magnetic flux in the coil increases, generating an induction current in the circular copper coil (ii). With a continuous rotation process, the separation distance between the coil and the magnet increases and the magnetic flux in the coil decreases, resulting in a reverse induction current (iii). Finally, the magnet rotates to the farthest position and the conduction current returns to zero (iv). With a periodic rotational motion, the EMG can generate a continuous AC. The magnetic field of the cylindrical magnet is also simulated by using Multiphysics COMSOL. The distribution of magnetic flux density surrounding the magnet can be observed in Figure 2d.

To optimize the output performance of the TENG component, the rotational speed, interdigital-electrode parameters, and the distance between PC fluff and FEP are investigated. A numerically-controlled electrical rotating machine is used for the test. The length of the PC fluff is ≈10 mm, and it is directly pasted on the acrylic disk. The effect of rotational speed on the electrical output performance of the T-TENG is first investigated. When the rotational speed increases from 10 to 150 rpm, the open-circuit (V_{OC}) and the transfer charges (Q_{SC}) are almost stable at 1.567 kV and 0.364 μC, and the short-circuit current (I_{SC}) increases from 0.224 to 6.359 μA (**Figure 3**a). The stable V_{OC} and Q_{SC} can be attributed to the operation mechanism that the transferred charges will maintain stable after reaching a saturation state, regardless of the rotation speed. For I_{SC}, as the time for charge transfer at a higher rotation speed will be shorter, the I_{SC} will increase when the rotation speed is increased (referring to the Equation 1).[27]

$$I = dQ/dt \tag{1}$$

In addition to the rotational speed, the number of interdigital electrodes is another crucial factor affecting the output performance of TENG. As illustrated in Figure 3d–f, the influence of the number of interdigitated electrodes (N = 3, 4, 6, and 8) on the triboelectric outputs has been tested. The V_{OC} and Q_{SC} of the T-TENG with N = 3 show the highest value of 1.535 kV and 0.362 nC, respectively. In contrast, the I_{SC} of T-TENG with N = 8 shows the highest value of 5.32 μA. These results can be attributed to the following reason. With the multiplication of electrode units, the effective contact area will be decreased to reduce the V_{OC} and Q_{SC}, and the time for charge transfer will be shortened and increase the I_{SC}.[28]

For the rotary structure T-TENG, the gap D between the rotor (acrylic disk with adhered PC fluff) and the FEP disk, which

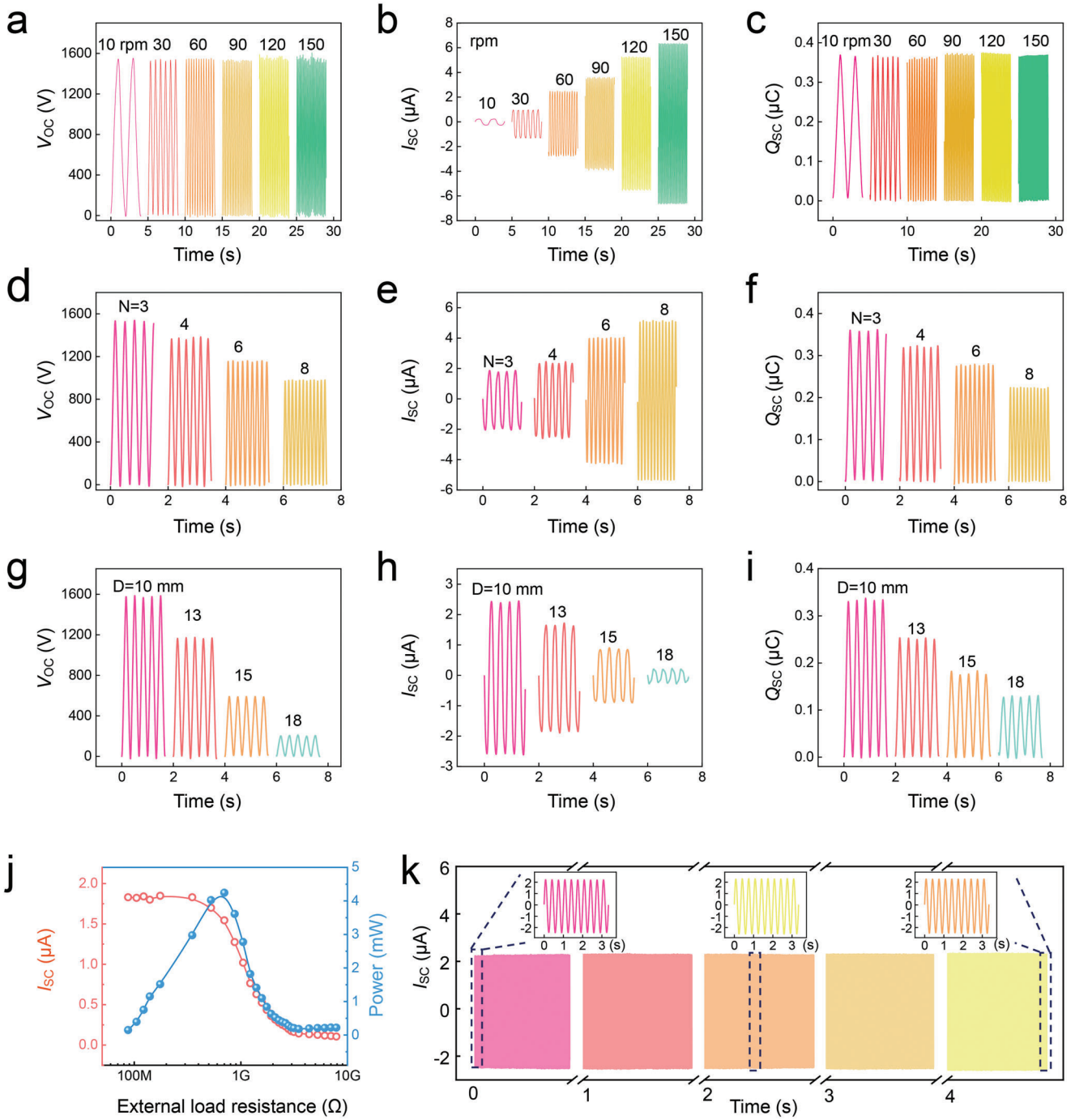

Figure 3. Structural design and optimization of rotary TENG. a) The open circuit voltage (V_{OC}), b) short current (I_{SC}), and c) transferred charge (Q_{SC}) waveforms at different speeds under the test conditions of rotating electrical machines. d) V_{OC}, e) I_{SC}, and f) Q_{SC} waveforms of the rotary TENG at the different numbers of interdigitated electrode pairs. g) V_{OC}, h) I_{SC}, and i) Q_{SC} waveforms of the rotary TENG with the different internal gaps between acrylic and FEP. j) Instantaneous peak current and power-resistance relationship profiles for the rotary TENG under the selected structural conditions (60 rpm, $N = 3$, $D = 10$ mm). k) Cyclic stability test of rotary TENG under selected structural conditions, the inset is the I_{SC} waveform in the early, middle, and end stages.

determines the degree of contact, is also an important parameter affecting the output performance of TENG. When the distance D decreases from 18 to 10 mm, the V_{OC} increases from 202 V to 1.571 kV (Figure 3g), the I_{SC} increases from 0.204 to 2.57 μA (Figure 3h), and the transferred charges increase from 0.127 to 0.336 μC (Figure 3i). The output performance can be improved by changing the separation distance or PC fluff length to obtain the optimal contact state. Meanwhile, it should be considered that the tight contact state will lead to excessive frictional resistance, so the distance can be adjusted on demand according to the actual driving force. After discussing the above-mentioned factors, the structure parameter of T-TENG can be decided to obtain the optimal output performance. Similarly, the relevant discussion on the lateral TENG parameter is shown in Figure S2 (Supporting Information).

The electrical outputs of the T-TENG with a load resistor are characterized to depict the peak current resistance and peak power resistance as shown in Figure 3j (rotation speed = 60 rpm, $N = 3$, and $D = 10$ mm). The instantaneous output power is calculated by:

$$P = I_t^2 \cdot R \tag{2}$$

where R is the resistance of the load resistor and I_t is the instantaneous current across the resistor. As shown in **Figure 4**j, the instantaneous peak power reaches its maximum value of 4.24 mW at the matched resistance of 700 MΩ. Figure 3k shows the cycle stability of the T-TENG in 4 h. By using PC fluff as one of the friction layers, the wear degree on the surface of FEP film can be greatly reduced because of the soft contact of the PC fluff membrane. Consequently, there is almost no remarkable decrease in the output performance after 45 000 cycles.

The structural design of the EMG and corresponding output performance are explored in Figure 4. Previous work has demonstrated the effect of magnet number on the output performance, indicating that arranging as many magnets as the device size allows can help to improve the output performance.[29] In this study, we have tried to fix six rectangular magnets in the EMG framework paired with three external rectangular coils. Figure 4a shows the COMSOL simulation of the distribution of magnetic induction lines when the magnetic poles of the magnet are arranged in the same direction (i) and arranged alternately (ii). Higher density of the magnetic induction lines can be observed in Figure 4a(i) for the situation of alternate arrangement of the magnets, which means the coils can cut more magnetic induction lines to generate a better output performance. Figure 4b,c compare the output performances for the two different cases, and it is clear that higher voltage and current outputs are obtained by placing the magnets in the same direction. And the output voltages and currents of the single coil are shown in Figure S3 (Supporting Information). In order to further optimize the output performance of EMG, we also compare the V_{OC} and I_{SC} when the three coils are connected in series and parallel, as shown in Figure 4d,e. The results show that higher V_{OC} and I_{SC} are obtained when the EMGs are connected in series and parallel, respectively. For further comparison, the charging capacity of the series and parallel-connected EMGs are compared by charging 47 μF capacitor through the rectifier circuit, respectively. Obviously, better-charging performance is obtained when the coils are connected in series, which is mainly because the voltage output of the EMG determines the saturation voltage of the capacitor. In addition to the above characterizations, we also build a test rig to test the effect of different speeds on the output performance by rotating the motor, as shown in Figure 4g and Figure S4 (Supporting Information). As the speed increases from 30 to 240 rpm, the voltage value increases from 0.51 to 3.54 V and the current increases from 1.34 to 6.43 mA. The V_{OC} and I_{SC} of EMG increase linearly with the rotating speed based on Faraday's induction law. The effect of the distance D between the magnet and the coil on the output performance of the EMG is also explored as shown in Figure 4h and Figure S5 (Supporting Information). As D increases from 5 to 15 mm, the output voltage drops from 0.99 to 0.11 V and the current drops from 2.54 to 0.404 mA. This is mainly attributed to that the magnetic induction strength is gradually decreased when D increases, consistent with Faraday's induction law. Meanwhile, the optimum load resistance and the peak output power of EMG are systematically studied at a rotation speed of 60 rpm. As illustrated in Figure 4i, the internal resistance of EMG (313 Ω) is smaller than that of the TENG (700 MΩ). From the calculation, the maximum peak power for EMG can reach 1.52 mW at an optimum load resistance of 315 Ω.

According to the above characterization and optimization, appropriate parameters are determined for the TENGs and EMG. **Figure 5**a shows the V_{OC}, I_{SC}, and Q_{SC} of the T-TENG and L-TENG under the wind speed of 15 m s^{-1}. The V_{OC}, I_{SC}, and Q_{SC} of the T-TENG are 1.44 kV, 8.74 μA, and 0.407 μC, respectively. And the V_{OC}, I_{SC}, and Q_{SC} of the L-TENG are 1.27 kV, 6.4 μA, and 0.342 μC, respectively. As shown in Figure 5b, the V_{OC} and I_{SC} of the EMG are 6.872 V and 18.64 mA, respectively. The optimum load resistance and the peak output power of EMG are studied under different wind speeds in Figure S6 (Supporting Information). Figure 5c summarizes their peak power under different wind speeds. The results indicate that when the wind speed increases from 5 to 25 m s^{-1}, both the peak powers of EMG and TENG show an increment tendency. It is obvious that the output power of TENG is low compared to EMG, and the output change of EMG with wind speed is more significant. Therefore, to further improve the charging efficiency of the TENG, an energy management circuit (EMC) that consists of a matched inductor and a spark switch is used.[30] The equivalent circuit diagram and optical photograph of the integrated EMC are shown in Figure 5d,c, in which the inductor serves as an energy storage unit when the switch is on and as an energy supply unit when the switch is off.[31,32] Based on the EMC, the charging efficiency of TENG can be effectively improved, as shown in Figure 5f. When L-TENG is used to charge a 330 μF capacitor with the EMC, it can charge the voltage to 6 V in 23 s. However, without the EMC, it needs to take 120 s to charge the capacitor to a lower voltage of 2 V. This result demonstrates that the introduction of EMC can significantly increase the charging efficiency by 15 times. The charging curves of the two TENGs in series and parallel conditions are compared in Figure S7 (Supporting Information). The TENGs connected in parallel can obtain higher charging efficiency. Subsequently, we try to use the two TENGs to charge different types of capacitors through the EMC. As shown in Figure 5g, the 1 mF capacitor can be rapidly charged to 7 V within 70 s. The results show that giant performance improvements of TENG systems can be achieved by matched inductor design. The designed EMC can

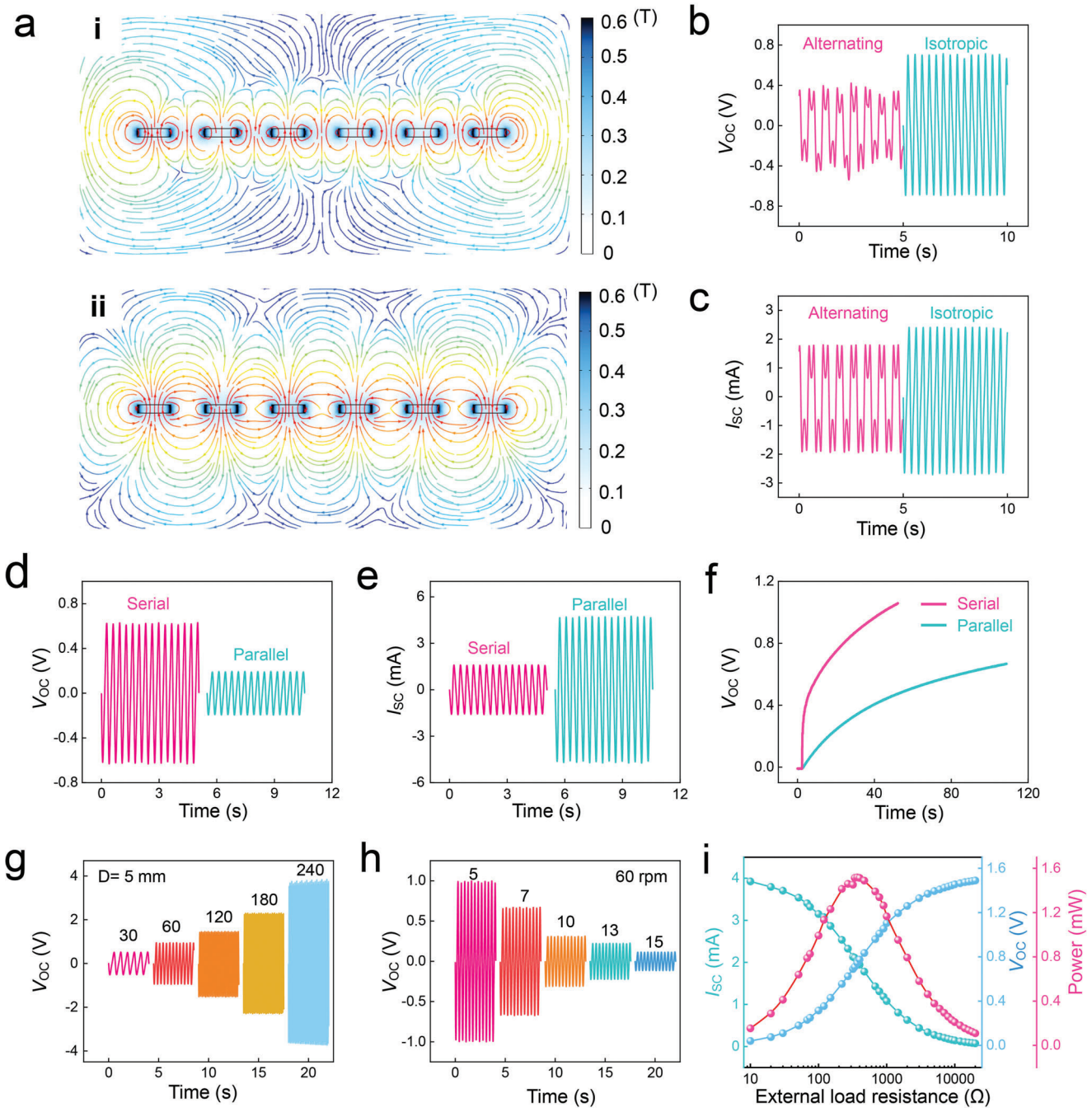

Figure 4. The principle and structure optimization of the EMG. a) COMSOL simulation of magnetic flux distribution in EMG with i) isotropic placement and ii) alternate placement of magnets. Comparison of the b) V_{OC} and c) I_{SC} in EMG with the isotropic and alternating placement of magnets (60 rpm). Comparison of d) V_{OC} and e) I_{SC} of three windings of EMG connected in series and parallel. f) Comparison of charging performance of 47 μF capacitor with three windings in series and parallel. g) The V_{OC} waveforms of the EMG with the different internal gaps between windings and magnets under the test conditions of rotating electrical machines. h) The V_{OC} waveforms of the EMG with the different rotary speeds under the test conditions of rotating electrical machines. i) Instantaneous peak V_{OC}, I_{SC}, and power-resistance relationship profiles for the EMG under the selected structural conditions.

facilitate TENGs to become the most competitive candidate for a distributed energy supplier by harvesting the surrounding low-frequency and disordered environmental energy. Figure 5h further shows the charging curves of a 1 mF capacitor by the TENG and EMG connected in parallel and series, respectively. TENG alone has the slowest charging efficiency, and it can charge to the maximum voltage quickly with only EMG. In contrast, the series connection of TENG and EMG leads to lower charging efficiency due to the impedance mismatch. The results show that the parallel connection of TENG and EMG can obtain higher energy output. This is because parallel connection TENG and EMG can charge the capacitor without interfering with each other and

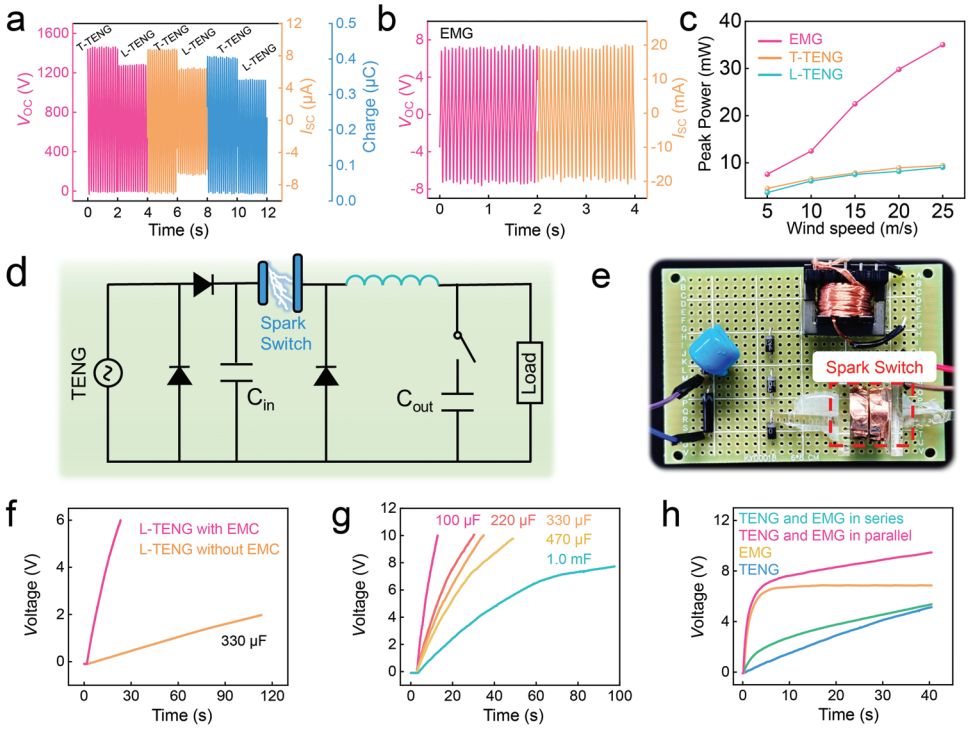

Figure 5. Testing of RS-HG charging performance. a) V_{OC}, I_{SC}, and Q_{SC} waveforms of T-TENG and L-TENG at a wind speed of 15 m s^{-1}. b) V_{OC} and I_{SC} waveforms of EMG at a wind speed of 15 m s^{-1}. c) Peak power of T-TENG, L-TENG, and EMG at different wind speeds. d) Equivalent circuit diagram of the integrated energy management circuit (EMC). e) Optical photograph of the integrated EMC. f) Comparison diagram of charging curve of 330 μF capacitor by L-TENG with and without EMC. g) Charging curve of different capacitors by L-TENG and T-TENG connected in parallel after EMC. h) Charging curve of a 1 mF capacitor that is powered by the TENG, the EMG, and two units connected in parallel and series, respectively (the wind speed is 15 m s^{-1}).

complement each other. The EMG works mainly during the first 5 s, and then the high voltage characteristics of the TENG help to continuously charge the capacitor.

According to the above investigations, the EMG has higher average output current and power, while the two TENGs have higher output voltage. Therefore, the hybridization of EMG and TENG offers a feasible way to effectively scavenge mechanical energy in the environment. **Figure 6**a shows the workflow diagram of the energy harvesting and power supply application. Equivalent circuit diagram of the RS-HG energy harvesting is presented in Figure 6b, in which the two TENGs and EMG are connected in parallel to charge the capacitor and then supply power to the consumer. As shown in Figure 6c and Movies S1–S3 (Supporting Information), the RS-HG can charge a 1 mF capacitor to 2 V or even 6 V with only a few rotation cycles and drive some common low-power appliances (e.g., stopwatch, calculator, and temperature and humidity sensor) to work for a long time. Figure 6d–f shows the corresponding photograph of powering the stopwatch, the calculator, and the temperature & humidity sensor. Benefiting from the high output performance of RS-HG, we have further demonstrated the application of RS-HG to charge high-power lighting lamps and even successfully charge smart phone through a voltage stabilizing circuit. As shown in Figure 6g and Movie S4 (Supporting Information), it takes ≈14 s to charge a 3 mF capacitor to 10 V. Figure 6h shows the photograph of driving lighting lamp by the RS-HG. The successful charging of the smartphone based on the step-down and voltage stabilization module is shown in Figure 6i, which presents the phone can be charged from 50% to 51% in ≈8 min (Figure S8 and Movie S5, Supporting Information).

3. Conclusion

In summary, we have demonstrated a high-performance hybrid nanogenerator for ocean wind energy harvesting by combining the high conversion efficiency of the TENG assisted with an energy management circuit and the high output performance of an EMG. By introducing the PC fluff structure in the rotary operation mode, the RS-TENG has excellent wear resistance and high voltage output to compensate for the low voltage disadvantage of EMG, which is important for better capturing the renewable wind energy in the environment. Besides, the utilization of the EMC with a matched inductor and a spark switch can significantly improve the conversion efficiency of TENG by 15 times. Based on the EMC, the demonstrated RS-HG can rapidly charge a 1 mF capacitor to 8 V within 15 s (under a wind speed of 15 m s^{-1}) and continuously power some electronic equipment. These results exhibit the potential applications of the RS-HG in self-powered environmental monitoring during ocean cruises. Furthermore, through the step-down and voltage stabilization module, the RS-HG can even successfully charge a smartphone to further expand its application scenarios and commercial prospects. This work offers an effective means of harvesting ocean wind energy with

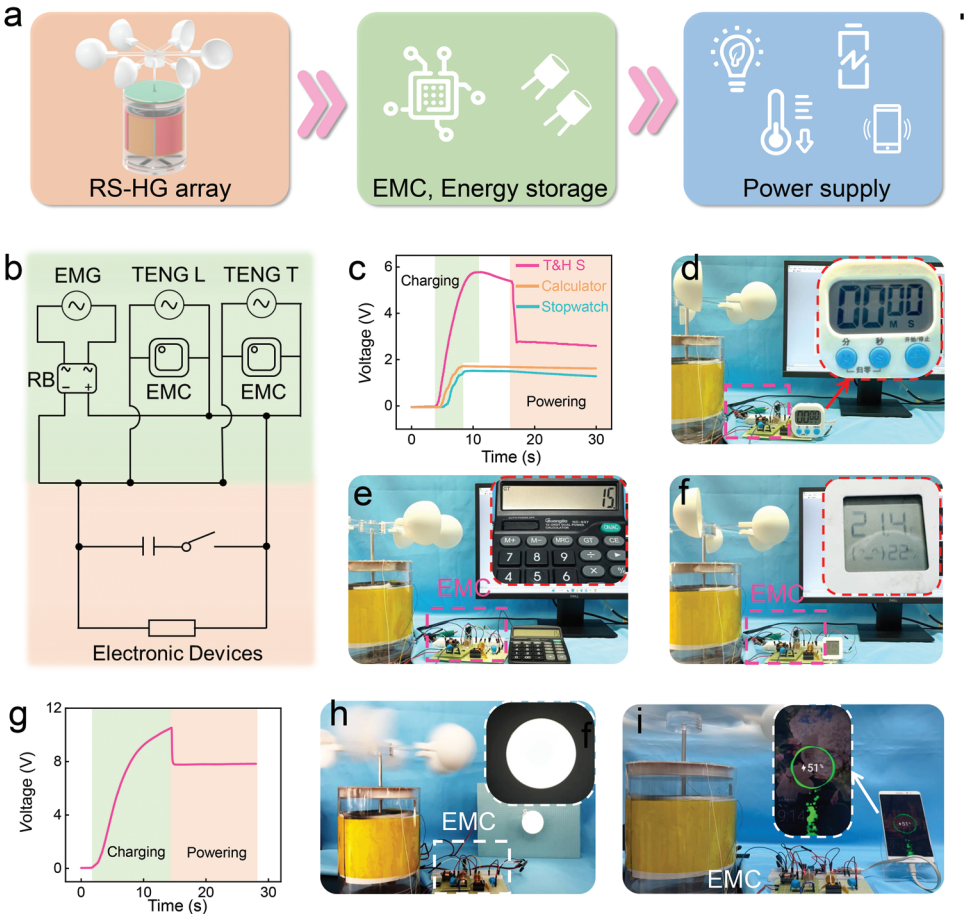

Figure 6. Demonstration of energy harvesting and power supply application by wind-driven RS-HG. a) Workflow diagram of energy harvesting and power supply application. b) Equivalent circuit diagram of RS-HG energy harvesting and power supply application (TENG and EMG connect in parallel). c) Charging curve of the stopwatch, calculator, and temperature & humidity sensor (1 mF capacitor). Photograph of powering d) the stopwatch, e) the calculator, f) the temperature and humidity sensor. g) Charging curve on 3 mF storage capacitor connected to the high-power bulb. h) Photograph of the continuously powered bulb. i) Photograph of charging a smartphone through the step-down and voltage stabilization module.

high efficiency, which has great potential for navigation applications and is facile to extend to multiple application scenarios.

4. Experimental Section

Fabrication of RS-TENG: The T-TENG and L-TENG were both composed of two parts: a stator and a rotator. The stator of the T-TENG was made up of a commercially printed circuit board (PCB) with six sectors shaped as triboelectric electrodes, whose diameter was 150 mm; the angle of each sector was 60°. The FEP film had a thickness of 50 μm that was fixed on the PCB as the triboelectric dielectric layer. The rotator was fabricated by an acrylic disk, and three sectored PC fluff with equal degree radially arrayed sectors were pasted on the acrylic substrate, the outer diameter and inner diameter of the sectored PC fluff were 150 and 20 mm, the length of the fiber was 10 mm. As for the L-TENG, the induction electrodes of the stator were three sets of forked finger electrodes cut by a laser cutting machine from conductive adhesive tape, FEP membrane was applied to the surface as a triboelectric dielectric layer. The rotor was made by a light-curing 3D printer, and three rectangular PC fluff membranes were glued to the side of the stator.

Fabrication of RS-EMG: The FB-EMG also consisted of two parts: a stator and a rotator. The stator was an acrylic disc with three equal-angle rectangles (20 × 60 mm) cut out by a laser cutting machine, in which the coil was placed, and an acrylic disk was placed on each side of the top and bottom for encapsulation. As for the rotor, similarly, six equal-angle rectangles (15 × 50 mm) were cut out of the acrylic disk by a laser cutter, six magnets were placed in them, and the top and bottom were each placed in the acrylic disc for encapsulation. Finally, L-TENG, T-TENG and EMG were assembled with bearings and aluminum rods, and the wind cups were printed by a 3D printer.

Characterization and Measurement: The electric outputs of the hybrid nanogenerator were tested by a programmable electrometer (Keithley Instruments model 6514). A stepper motor (86HSE8.5N, China) was used to drive the TENG and EMG when testing different rotating speeds. The simulated wind was generated by the blower.

Supporting Information

Supporting Information is available from the Wiley Online Library or from the author.

Acknowledgements

This work was financially supported by the National Key Research and Development Program of China (2021YFB3200304), the National

Natural Science Foundation of China (52073031), the Beijing Nova Program (Z211100002121148), the Fundamental Research Funds for the Central Universities (E0EG6801×2), the "Hundred Talents Program" of the Chinese Academy of Sciences, and the Guizhou Provincial Science and Technology Foundation (ZK [2022] General 112).

Conflict of Interest

The authors declare no conflict of interest.

Data Availability Statement

The data that support the findings of this study are available from the corresponding author upon reasonable request.

Keywords

blue energy, energy management circuits, hybrid nanogenerators, wind energy harvesting, triboelectric nanogenerators

Received: March 1, 2023
Revised: April 18, 2023
Published online: May 23, 2023

[1] L. Chu, S. Zhai, W. Ahmad, J. Zhang, Y. Zang, W. Yan, Y. Li, *Nano Res. Energy* **2022**, *1*, e9120024.
[2] B.-G. Paik, S.-R. Cho, B.-J. Park, D. Lee, B.-D. Bae, J.-H. Yun, *J. Mar. Sci. Technol.* **2009**, *14*, 115.
[3] S. Zhang, L. Sun, Q. Fan, F. Zhang, Z. Wang, J. Zou, S. Zhao, J. Mao, Z. Guo, *Nano Res. Energy* **2022**, *1*, e9120001.
[4] H. Xue, H. Gong, Y. Yamauchi, T. Sasaki, R. Ma, *Nano Res. Energy* **2022**, *1*, e9120007.
[5] Z. L. Wang, *Nano Energy* **2019**, *58*, 669.
[6] X. Cao, X. Wei, R. Li, Z. Wang, Z. Wu, *Nano Res.* **2022**, *16*, 2502.
[7] X. Cao, Y. Xiong, J. Sun, X. Zhu, Q. Sun, Z. L. Wang, *Adv. Funct. Mater.* **2021**, *31*, 2102983.
[8] K. Wang, W. Xu, W. Zhang, X. Wang, X. Yang, J. Li, H. Zhang, J. Li, Z. Wang, *Nano Res. Energy* **2023**, *2*, e9120042.
[9] Z. L. Wang, *Adv. Energy Mater.* **2020**, *10*, 2000137.
[10] Y. Yang, G. Zhu, H. Zhang, J. Chen, X. Zhong, Z. H. Lin, Y. Su, P. Bai, X. Wen, Z. L. Wang, *ACS Nano* **2013**, *7*, 9461.
[11] F.-R. Fan, Z.-Q. Tian, Z. Lin Wang, *Nano Energy* **2012**, *1*, 328.
[12] H. S. Liu, J. Cao, S. Feng, G. G. Cheng, Z. Q. Zhang, J. N. Ding, *Adv. Mater. Technol.* **2023**, *8*, 202201766.
[13] S. Li, D. Liu, Z. Zhao, L. Zhou, X. Yin, X. Li, Y. Gao, C. Zhang, Q. Zhang, J. Wang, Z. L. Wang, *ACS Nano* **2020**, *14*, 2475.
[14] X. Liang, T. Jiang, Y. W. Feng, P. J. Lu, J. An, Z. L. Wang, *Adv. Energy Mater.* **2020**, *10*, 2002123.
[15] X. Cao, Y. Xiong, J. Sun, X. Xie, Q. Sun, Z. L. Wang, *Nano-Micro Lett.* **2022**, *15*, 14.
[16] J. Cao, Y. Lin, X. Fu, Z. Wang, G. Liu, Z. Zhang, Y. Qin, H. Zhou, S. Dong, G. Cheng, C. Zhang, J. Ding, *Nano Energy* **2023**, *107*, 108150.
[17] C. Ye, K. Dong, J. An, J. Yi, X. Peng, C. Ning, Z. L. Wang, *ACS Energy Lett.* **2021**, *6*, 1443.
[18] P. Wang, L. Pan, J. Wang, M. Xu, G. Dai, H. Zou, K. Dong, Z. L. Wang, *ACS Nano* **2018**, *12*, 9433.
[19] H. Guo, Z. Wen, Y. Zi, M.-H. Yeh, J. Wang, L. Zhu, C. Hu, Z. L. Wang, *Adv. Energy Mater.* **2016**, *6*, 1501593.
[20] P. Lu, H. Pang, J. Ren, Y. Feng, J. An, X. Liang, T. Jiang, Z. L. Wang, *Adv. Mater. Technol.* **2021**, *6*, 2100496.
[21] Z. Wu, Z. Cao, R. Ding, S. Wang, Y. Chu, X. Ye, *Nano Energy* **2021**, *89*, 106425.
[22] C. Han, Z. Cao, Z. Yuan, Z. Zhang, X. Huo, L. a. Zhang, Z. Wu, Z. L. Wang, *Adv. Funct. Mater.* **2022**, *32*, 2205011.
[23] H. Zou, Y. Zhang, L. Guo, P. Wang, X. He, G. Dai, H. Zheng, C. Chen, A. C. Wang, C. Xu, Z. L. Wang, *Nat. Commun.* **2019**, *10*, 1427.
[24] J. Han, Y. Feng, P. Chen, X. Liang, H. Pang, T. Jiang, Z. L. Wang, *Adv. Funct. Mater.* **2021**, *32*, 2108580.
[25] P. Chen, J. An, R. Cheng, S. Shu, A. Berbille, T. Jiang, Z. L. Wang, *Environ. Sci.* **2021**, *14*, 4523.
[26] B. Zhang, S. Zhang, W. Li, Q. Gao, D. Zhao, Z. L. Wang, T. Cheng, *ACS Nano* **2021**, *15*, 20278.
[27] Y. Luo, P. Chen, L. N. Y. Cao, Z. Xu, Y. Wu, G. He, T. Jiang, Z. L. Wang, *Adv. Funct. Mater.* **2022**, *32*, 2205710.
[28] S. Yong, H. Wang, Z. Lin, X. Li, B. Zhu, L. Yang, W. Ding, R. Liao, J. Wang, Z. L. Wang, *Adv. Energy Mater.* **2022**, *12*, 2202469.
[29] F. Zheng, Y. Zhou, S. Hu, R. Li, Z. L. Wang, Z. Wu, *Adv. Energy Mater.* **2022**, *12*, 2201966.
[30] Z. Wang, Q. Tang, C. Shan, Y. Du, W. He, S. Fu, G. Li, A. Liu, W. Liu, C. Hu, *Environ. Sci.* **2021**, *14*, 6627.
[31] H. Zhou, X. Wei, B. Wang, E. Zhang, Z. Wu, Z. L. Wang, *Adv. Funct. Mater.* **2022**, *33*, 2210920.
[32] Z. Wang, W. Liu, W. He, H. Guo, L. Long, Y. Xi, X. Wang, A. Liu, C. Hu, *Joule* **2021**, *5*, 441.